Correlation between eddy currents and corrosion in electric submersible pump systems

I.A. Metwally *, A. Gastli

Department of Electrical & Computer Engineering, College of Engineering, Sultan Qaboos University, Sultanate of Oman

Abstract

This paper introduces both stray magnetic-field and thermal analyses of electric submersible pump (ESP) motors and cables under normal and abnormal operating conditions. These abnormal operating conditions include running the electric submersible pump motor under imbalance and single-phasing. Moreover, both concentric and eccentric electric submersible pump oil well models with flat and round cables were investigated. Experimental tests were conducted on a reduced-scale electric submersible pump motor. In addition, theoretical simulations were performed using a finite-element based software package for a reduced-scale electric submersible pump motor, and a full-scale electric submersible pump motor and its power cable of flat and round types. Compared to the cases of running the motor under balanced or unbalanced conditions, the single-phasing operation of eccentric wells gives the highest localized magnetic-flux and eddy current densities, hence the possibility of localized corrosion increases. It has been found that there is a strong correlation between the eddy-current thermal effect and the severe localized corrosion of the electric submersible pump system. Therefore, it is highly recommended to use round power cables and not to operate the electric submersible pump system under single phasing conditions.
© 2007 Elsevier Masson SAS. All rights reserved.

Keywords: Corrosion; Electric submersible pump motor; Cable; Eddy current; Thermal analysis; Magnetic analysis; Eccentricity; Imbalance; Single phasing

1. Introduction

Corrosion is becoming an increasing threat to the integrity of oil field structures including pipelines, well casing and tubing world wide [1], where downhole logs of some well casings showed corrosion rates often higher than 2 mm/year. Basically, there are four types of corrosion that can occur [2–6], namely, general corrosion (chemical in nature), concentration cell corrosion (electrochemical cell caused by differences in the electrolyte), galvanic corrosion (electrochemical cell caused by differences in the metal), and stray current corrosion (electrochemical cell caused by external electrical sources). Stray electrical currents (both AC and DC) were felt to be a significant cause of corrosion in many industrial applications [2–5]. Stray current corrosion (SCC) is the most severe form of corrosion because the metallic structure is forced

to become an anode and the amount of current can be translated directly into metal loss. One ampere of DC current discharge from a pipeline for one year may consume 10 kg of steel [4].

During the last two decades, a modern pumping method using electrical submersible pump system has been developed in the oil industry [7]. Basically, it consists of a pump driven by an induction motor located downhole the oil well via a long power cable with a length ranges from 1 km to 3 km. This system doesn't require any gas injection. The electric submersible pump system is considered as an effective, economical and environment-friendly mean of lifting large volumes of oil [7]. The excessive corrosion rate of such electric submersible pump system has become a concern in recent years. Several factors contributed to electric submersible pump failures due to corrosion. Fig. 1 illustrates a typical example of severe localized corrosion of electric submersible pump motors in an oil field. These failures have a very high cost because electric submersible pump's failures result in oil production losses or what is so-called "oil deferment" affecting revenue, and pulling out

* Corresponding author. Tel.: +4989 60043940; fax: +4989 60043723.
E-mail address: Ibrahim.Metwally@unibw.de (I.A. Metwally).

Fig. 1. Examples of severe localized corrosion of electric submersible pump motor casing.

the motor from downhole requires mobilization of a rig, which has very high renting cost.

This paper focuses on investigating the different possible causes of corrosion-rate increase on the tubing, and the motor and well casings due to thermal effect of eddy currents and high magnetic field density.

2. Mathematical model of eddy currents

Eddy-current induced heating process of paramagnetic material is a well known phenomenon [8–15]. Eddy-current induced in a thin layer of a metallic surface gives rise to a heat flux. If the penetration region for the current is small enough, the heat flux may be assumed to be applied to the surface of the metal [16].

The mathematical model for the sinusoidal quasi-static eddy-current problem resulting from the Maxwell's equations is described by the complex magnetic vector potential $\vec{\underline{A}}$ and an electrical complex scalar potential $\underline{\phi}$ [10].

$$\nabla \times \left(\frac{1}{\mu} \nabla \times \vec{\underline{A}} \right) - \nabla \left(\frac{1}{\mu} \nabla \cdot \vec{\underline{A}} \right) + \sigma (j\omega \vec{A} + \nabla \underline{\phi})$$
$$= \vec{\underline{J_o}} = \sigma \vec{\underline{E_s}} \tag{1}$$

where j is the complex notation, $\vec{\underline{J_o}}$ is the supplied current density, $\vec{\underline{E_s}}$ is the electric field strength impressed by the power

source, μ is the permeability, σ is the electrical conductivity, and ω is the power angular frequency. It is worth mentioning that for 2D analysis $\nabla \cdot \vec{\underline{A}} = 0$. The requirement of zero divergence condition of current density must be fulfilled with Coulomb gauge [10]:

$$\nabla \cdot \left(\sigma (j\omega \vec{\underline{A}} + \nabla \underline{\phi}) \right) = 0 \tag{2}$$

Eqs. (1) and (2) are also known as the $\vec{\underline{A}} - \underline{\phi}$ formulation. The expression for current density is:

$$\vec{\underline{J}} = \sigma \vec{E_s} - \sigma (j\omega \vec{\underline{A}} + \nabla \underline{\phi}) \tag{3}$$

It determines the heat source (joule heat or specific power loss) distribution:

$$p_v = \frac{|\vec{\underline{J}}|^2}{\sigma} \tag{4}$$

The time-dependent Fourier temperature equation gives temperature field T in the material as a function of the eddy-current density by [12,13]:

$$\frac{\partial (c_p \rho_m T)}{\partial t} = p_v + \nabla \cdot (k \nabla T) = \frac{|\vec{\underline{J}}|^2}{\sigma} + \nabla \cdot (k \nabla T) \tag{5}$$

where c_p is the specific heat, ρ_m is the mass density, and k is the thermal conduction coefficient. As time progresses, the temperature rises accumulate in localized spots where the eddy-current density is very high. Therefore, the increased eddy-current densities on the motor and well casings, resulting from motor eccentricity and/or phase imbalance, lead to thermal excursions and localized excessive spike temperature rises at their surfaces. These thermal excursions and spikes are known to favor and to accelerate steel corrosion [16–18]. In [18], it was shown that even a couple of infrequent high-temperature thermal excursions, which can also lead to scale damage of carbon steel, followed by long post spike exposure may lead to a higher corrosion rate than its equivalent isothermal condition.
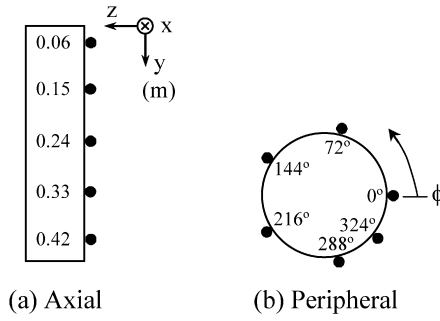
Fig. 2. Location of temperature sensors fixed at the motor casing.

The resultant mmf waveform at any point in the air gap of a 3-phase wound rotating machine can be defined by an angle ϕ, the number of turns per phase N, and the phase currents i_a, i_b and i_c. For a balanced case, the resultant mmf is as follows [19]

$$F_3(\phi) = F_a(\phi) + F_b(\phi) + F_c(\phi)$$
$$= Ni_a \cos\phi + Ni_b \cos(\phi - 120°)$$
$$+ Ni_c \cos(\phi + 120°) \tag{6}$$

The phase currents i_a, i_b and i_c are functions of time thus

$$F_3(\phi) = NI_m \cos\omega t \cos\phi$$
$$+ NI_m \cos(\omega t - 120°)\cos(\phi - 120°)$$
$$+ NI_m \cos(\omega t + 120°)\cos(\phi + 120°)$$
$$= 1.5NI_m \cos(\phi - \omega t) \tag{7}$$

where I_m is the current amplitude. Therefore, the resultant magnetic field is a rotating one, while in the case of single-phase operation, i.e. phase C is opened ($i_c = 0$), then the current in the other phases becomes

$$i_a = -i_b = \sqrt{3}I_m \cos(\omega t) \tag{8}$$

The latter case leads to a pulsating and localized magnetic filed which can cause significant mass transport, i.e. it accelerates the corrosion on the motor casing and the well casing, too. For the single-phase case, the resultant mmf waveform at any point in the air gap yields

$$F_1(\phi) = 1.5NI_m \cos(\omega t)\left(\sqrt{3}\cos(\phi) - \sin(\phi)\right) \tag{9}$$

3. Experimental setup

A reduced-scale water electric submersible pump was used which has the following [20]: 3-phase motor, 58 Hz, 3 kW, 415 V, 8.10 A (max), 0.73 power factor, 2875 rpm, 0.5 m axial length, 0.095 m diameter, and its pump has 0.83 m axial length and 0.089 m diameter. Ten adhesive temperature sensors (the overall accuracy with their data logger is $\pm1\%$) were fixed to the motor casing vertically along the axial length (5 sensors) and around its circumference (6 sensors) at an axial length $y = 0.24$ m to measure the temperature profiles at the 10 points simultaneously as shown in Fig. 2. The three-dimension (3-D) magnetic flux density components (B_x "tangential", B_y "axial", B_z "radial") were measured by 3-D sensors having a sensitivity of 0.1 mT/V and with a measurement range of ±1 mT
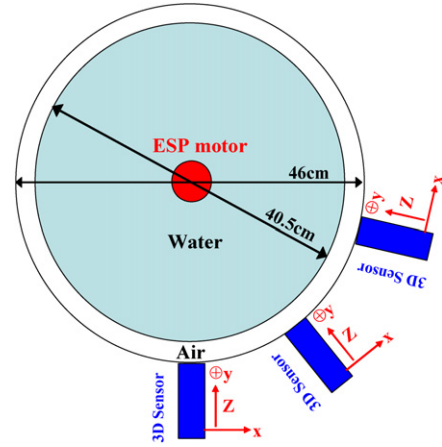

Fig. 3. Schematic representation of the peripheral scan of the magnetic flux densities.

Table 1
Input currents to the electric submersible pump motor

Operation	Three-phase current rms values (A)		
	Phase A	Phase B	Phase C
Balance	6.6	6.6	6.6
Imbalance	7.9	6.6	5.2
1-Phasing	11.43	11.43	0

(with an offset error of ±50 nT and a calibration accuracy of $\pm0.5\%$) [21] under different operating conditions of the motor. The electric submersible pump was submersed in a plastic tank then an axial and a peripheral scans of the 3-D magnetic flux density components were done under different operating conditions of the motor. Fig. 3 illustrates the peripheral scan, and Table 1 gives the input currents to the motor in rms and for various operating conditions. It can be noticed that phase C current was reduced and interrupted during the imbalance and single-phasing condition, respectively.

4. Experimental results and discussion

4.1. Temperature

An eddy current is a swirling current set up in a conductor in response to a time-varying magnetic field. Since the motor casing material is resistive, ohmic power losses are generated by the eddy current and appear as a heat on the casing surface. The main aim of this section is to measure the temperature profiles under balance, imbalance and single-phase operating conditions.

Fig. 4 shows that the temperature for the single-phase condition is the highest compared to the other two conditions that is due to the following of high current in some of the motor windings which assists the increase of the eddy currents. Therefore, more power loss will be converted into heat. Moreover, the temperature in the imbalance case is higher than that in the balance. The temperature profiles at height $y = 0.24$ m in Fig. 5 is also the highest for the single-phasing condition.
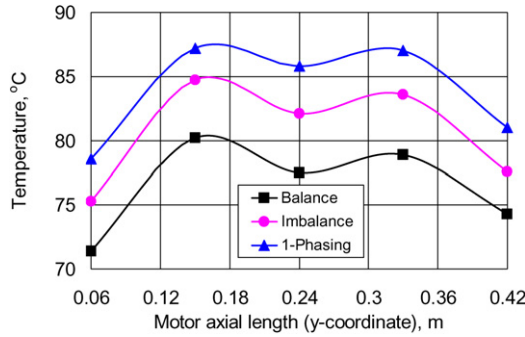
Fig. 4. Temperature profiles along the motor axial length for three operating conditions for $\phi = 0°$ and at $t = 960$ s.
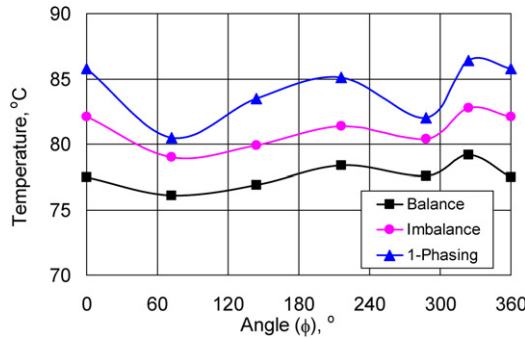

Fig. 5. Temperature profiles around the motor circumference for three operating conditions for $y = 0.24$ m and at $t = 960$ s.
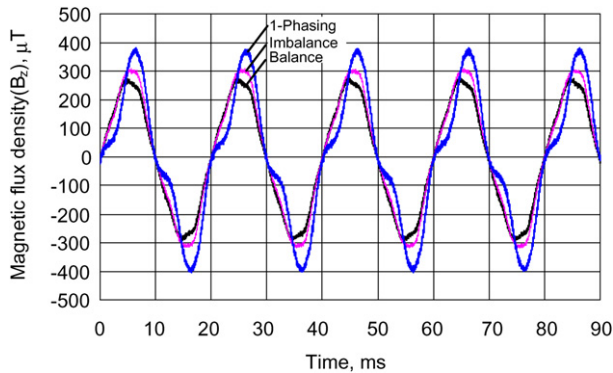

Fig. 6. Oscillograms of B_z under different operating conditions at $y = 0.24$ m and $\phi = 144°$.

4.2. Profiles of magnetic flux densities

4.2.1. Axial scan

The 3D components of the magnetic-flux density (B_x "tangential", B_y "axial", B_z "radial") were instantaneously measured for the aforementioned three operating conditions using a 3D magnetic-flux density sensor [21]. Small portion of the magnetic flux that is produced by flowing current through coils is leaked around the motor casing.

Fig. 6 illustrates the oscillograms of the z-component (radial) magnetic-flux density for different operating conditions at $y = 0.24$ m and $\phi = 144°$. It can be seen that the single-phase and the balance conditions give the highest and the lowest peak values, respectively.
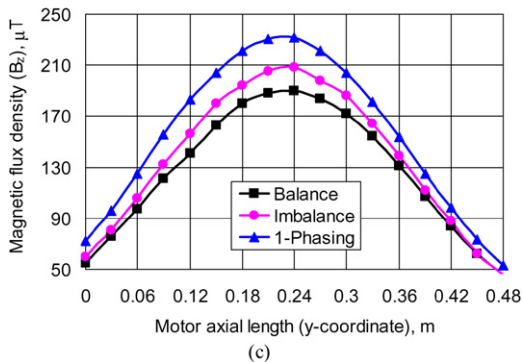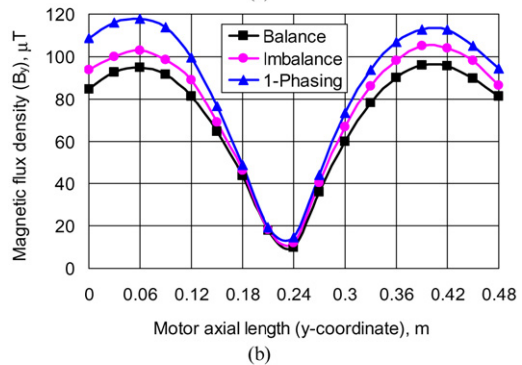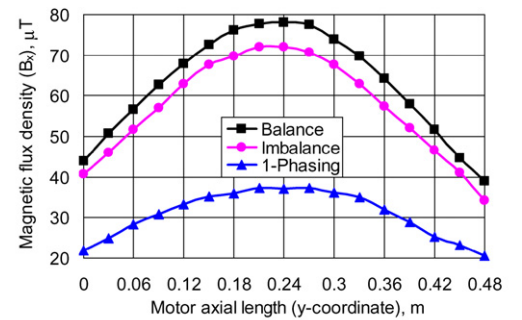

Fig. 7. Profiles of magnetic flux-density components versus the motor axial length for three operating conditions at $\phi = 144°$: (a) B_x, (b) B_y and (c) B_z.

Fig. 7(a) shows that the tangential magnetic-flux density in x-direction (B_x) has its peak in the middle of the motor axial length ($y = 0.24$ m).

The main reason behind this is the concentration of the magnetic flux produced by the parallel conductors "coil sides". The magnetic-flux density of the balanced condition is the highest, because this tangential component (B_x) mainly results from the currents in the coil sides in z-direction, where these coils mainly exist in the y–z plane. The trend of these results is also attributed to the fact that phase C current is reduced and interrupted during the imbalance and single-phasing condition, respectively (see Table 1). Fig. 7(b) shows that the magnetic flux density in y-direction (B_y) increases near the top and the bottom ends of the motor. This is due to the configuration of the winding "overhang effect". Both the B_x and the B_z components (shown in Figs. 7(a) and 6(c), respectively) have peak values at the middle of the motor length, where the radial component (B_z) is the highest. This component assists the mass transport significantly because it is perpendicular to the motor casing, and hence the higher this component the faster is
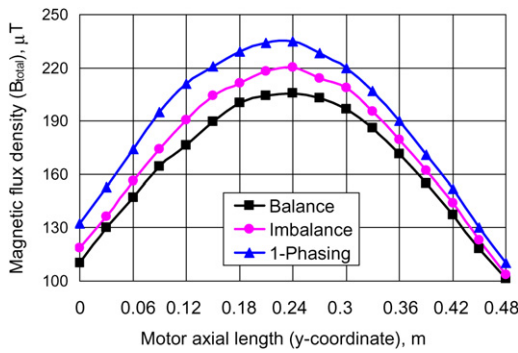
Fig. 8. Profiles of total magnetic flux-density versus the motor axial length for three operating conditions $\phi = 144°$.
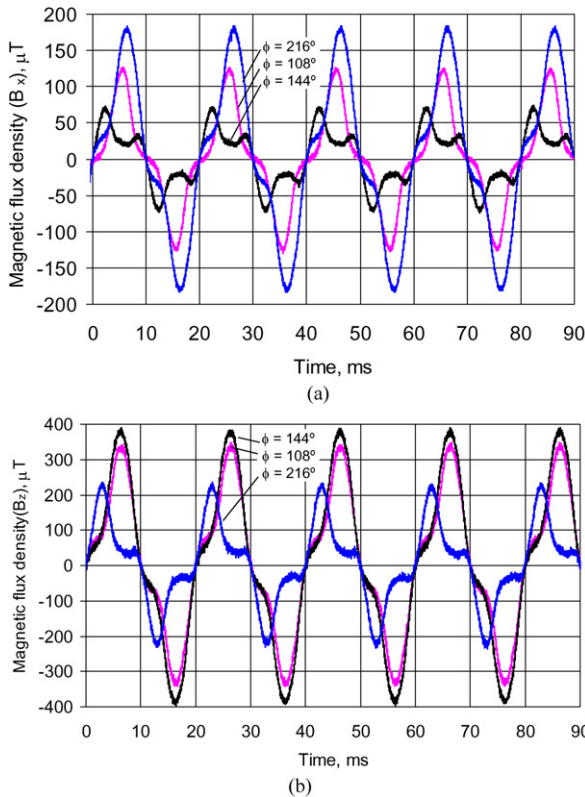

Fig. 9. Oscillograms of the x- and z-components of the magnetic flux density for single-phase operation at $y = 0.24$ m: (a) B_x and (b) B_z.
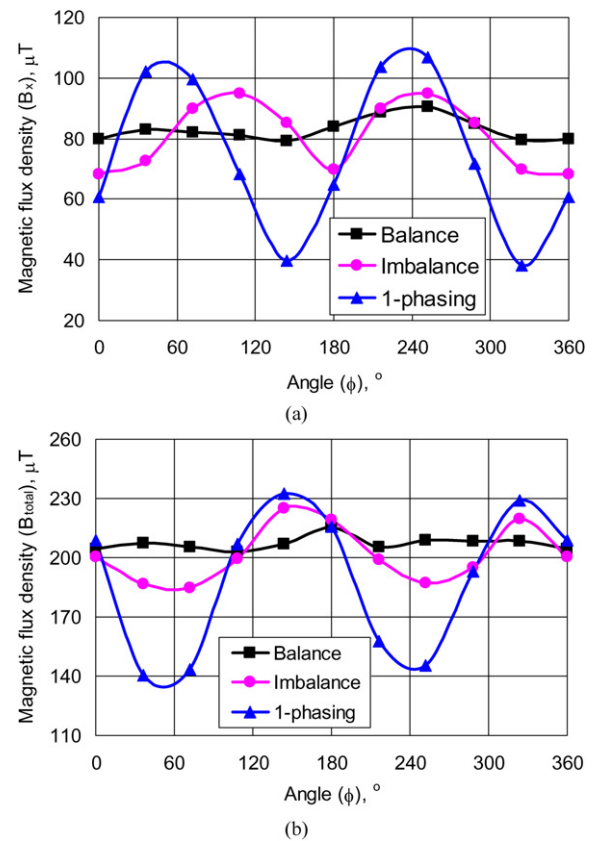

Fig. 10. Profiles of magnetic flux-density around the circumference at $y = 0.24$ m: (a) B_x and (b) B_{total}.

the single-phase operation at $y = 0.24$ m. At $\phi = 216°$, the B_x component is the highest, while the B_z component is the lowest.

The former is attributed to the fact that the coils which are perpendicular to the x-direction have a higher currents by $\sqrt{3}$. On the other hand, these coils which are exactly perpendicular to the z-direction have no currents (phase C), but the inclination of the coils of the other phase gives low B_z. It is worth mentioning that the y-component (parallel to the motor's axial length) was found very small.

The magnetic flux densities around the circumference can be obtained by making peripheral scan at the axial point $y = 0.24$ m. It can be seen from Fig. 10(a) that the x-component of the magnetic flux density reaches its maximum at two points. This is due to the variations of stator magnetic-flux density strength around its circumference as a result of high localized magnetic-flux density generated by the high current ($\sqrt{3}$ times the normal current for balanced case). This trend interprets the severe localized corrosion of electric submersible pump motors as shown in Fig. 1. Fig. 10(b) shows two minima and two maxima points which appear in the profiles of magnetic flux density around the circumference. This is because the stator of the motor consists of a 2-pole winding that split into two parts where the points of maxima appear. On the other hand, the points of minima appear in the gap between these windings. The results has also revealed that the $B_{total} \approx B_z$ which is consistent with those shown in Figs. 7 and 8.

the corrosion rate. Operating the motor under imbalance or single-phase condition leads to a reduction in the current flowing through these coils or even no current as for the case of single-phase condition. Since the total magnetic flux amplitude is $B_{total} = \sqrt{B_x^2 + B_y^2 + B_z^2} \approx B_z$, the total magnetic flux density curve takes the shape of the magnetic flux density in the z-direction as can be seen in Fig. 8.

4.2.2. Peripheral scan

The magnetic-flux density components around the electric submersible pump motor (peripheral scan) at a radius of 0.36 m and an axial length $y = 0.24$ m (middle of the motor height) were measured. Figs. 9(a) and 9(b) illustrate the recorded oscillograms of the B_x and the B_z components, respectively, for
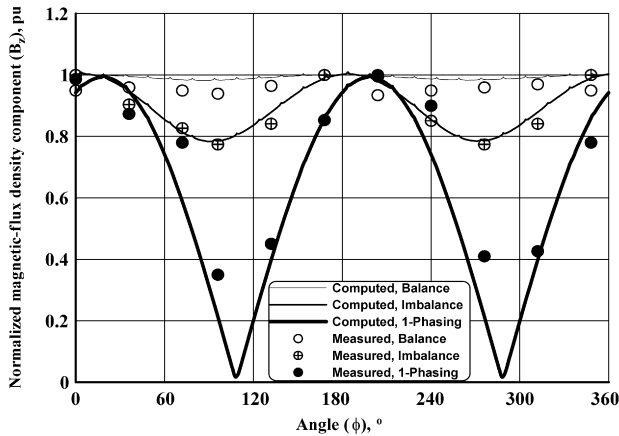
Fig. 11. Comparison between the measured (symbols) and computed (lines) profiles of magnetic flux-density component (B_z) around the circumference at $y = 0.24$ m.

Fig. 12. Electric submersible pump well system basic model (dimensions are in m).

In such magnetic-flux density measurements, there are many interference sources, e.g. the background magnetic field "the earth's magnetic field", the motor leads and the limited length of the motor (0.5 m). Therefore, the comparison between the measured and the computed magnetic flux-density was done in a normalized way to eliminate such errors as can be seen in Fig. 11. Notice that, for the different operating conditions, a good agreement has been obtained between the measured and the computed normalized magnetic flux-density component in z-direction "radial", i.e. B_z.

5. 2D finite-element modeling

Several 2D finite-element models of the electric submersible pump system are needed for the analysis of the electric submersible pump system design and operation under different possible conditions. The VectorField™ Opera-2D software package [22] is used for modeling and simulating the 2D electric submersible pump system.

Figs. 4 and 8 show that the profiles of the motor surface temperature and the total magnetic-flux density decrease near to the motor ends. Hence, it is not worth to calculate the eddy currents in axial direction using 3D FEM.

5.1. Oil well with electric submersible pump motor

The basic model of the electric submersible pump well system, including the motor, oil and well casing, is shown in Fig. 12. From the central part and moving out radially, there are the: rotor shaft, rotor core, rotor cage, airgap, stator windings (coils), stator core, motor casing, oil (fluid) mixture, well casing, and cement.

For the present 2D finite-element modeling, the numbers of elements, nodes and regions were set as 31 291, 16 244 and 22, respectively. Firstly, the meshes were automatically refined. Then, in order to increase the computation accuracy, the meshes were manually refined for the motor and the well casings.

All boundary conditions were set to fixed derivative type by OPERA-2D. The currents in the rotor are calculated and taken
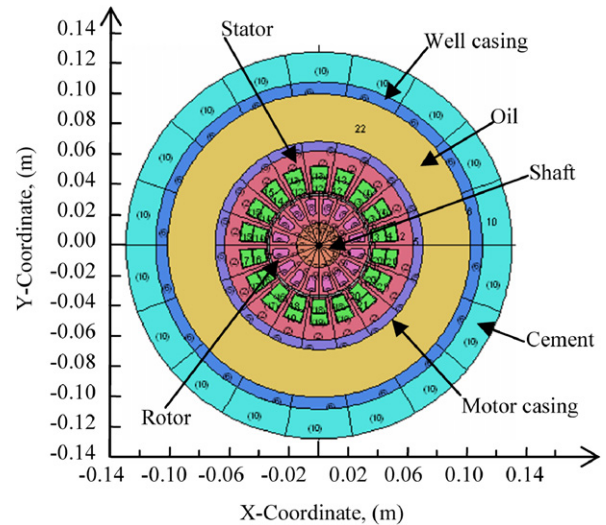
Table 2
Electric submersible pump system typical parameters

Part	Material	Conductivity (σ) MS/m	Relative permeability (μ_r)
Rotor bars	Aluminum	38.2	1
Stator winding	Copper	57.0	1
Rotor shaft	Steel	2.58	602
Rotor core	Electric steel	1.61	5000
Stator core	Electric steel	1.61	5000
Airgap	Air	0	1
Motor casing	Steel	2.58	602
Well casing	Steel	2.58	602
Oil (fluid mixture)	Oil, gas, sand and water	1	1

into account automatically. Calculations were done at standstill condition. The value of the stator currents frequency is 50 Hz, and the number of iterations was 749.

Because of confidentiality problems it is not possible for the authors to acquire actual accurate and detailed parameters of a typical electric submersible pump system design and construction from any electric submersible pump vendor. Typical topology and dimensions can only be approximated from the available literature and in consultation with some oil companies. This approximation can be considered sufficiently accurate to build a basic typical model for the electric submersible pump system using the Opera-2D software pre-processor.

The typical parameters were taken from the literature [23] and are listed in Table 2. Note that the data used were chosen arbitrary as a sample only. Note also that the oil was considered as a mixture of salted water, gas, and sand which gives it a slightly conducting property. The selected typical well casing diameter is 0.21 m and the motor casing diameter is 0.14 m.

It is well known that the electric submersible pump motors are normally operated near to the saturation zone of their B–H curve; hence 1% voltage imbalance results in up to 10% current imbalance [24]. Several cases of stator current imbal-
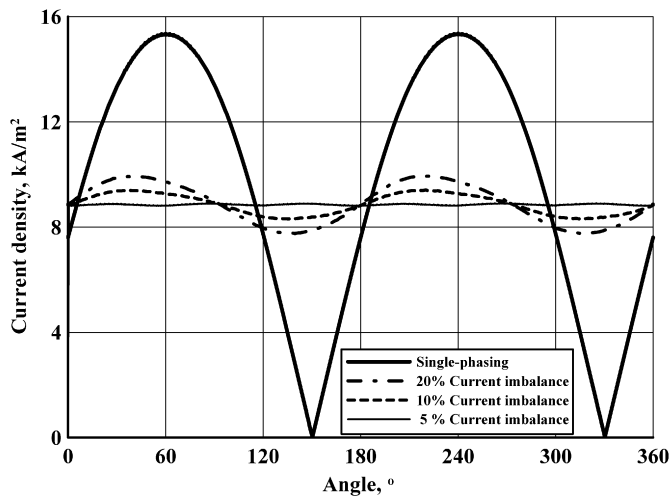
Fig. 13. Profile of eddy-current density on well casing as a function of current imbalance.
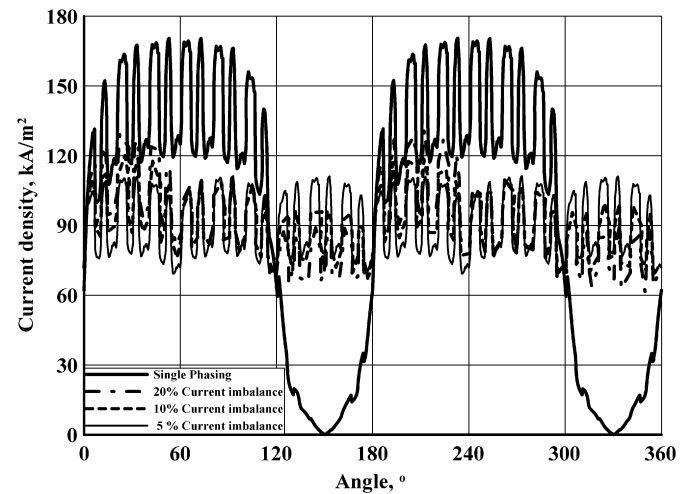

Fig. 14. Profiles of eddy-current density on motor casing as a function of current imbalance.

ance were investigated, namely, 10%, 15%, 20% and 100% (single-phasing). Fig. 13 shows the eddy-current density variation along the inner circumference of the well casing for the balanced, 10% and 20%, and 100% imbalance (single-phase) operations. From Fig. 13, one can notice that the higher the current imbalance, the higher is the eddy-current density in some localized places around the well casing.

For the three unbalanced conditions, the peaks do not coincide because the higher the current imbalance, the higher are the induced magnetic field and the eddy-current density and the more is the shift in the axis of the total magnetic-flux density. On the other hand, the current of the severest imbalance condition (single-phasing case) goes to zero in one phase on the expense of increasing the current in the other two phases by $\sqrt{3}$ for driving a constant power load. Therefore, the eddy-current densities opposite to this phase decay to zero at angles of 150° and 330°. The severest case is obtained for single-phase operation for which the maximum eddy current is about $\sqrt{3}$ times that of normal operation (balanced case), and so does the eddy-current density as shown in Fig. 13. The quasi-sinusoidal nature of variation for unbalance cases are also attributed to the same trend, where the current imbalance means the increase of the current in one or two phase and decrease it in the third one.

Similar trend of the eddy-current density has been observed on the motor casing as can be seen in Fig. 14. The effect of slots and teeth can be also noticed on these profiles, where the eddy-current density profile is so much pulsating on motor casing as compared to that on the well casing, and is much higher at the motor casing by about 11 times. Compared to the balanced condition, the peak value of the eddy-current density increases for the 10% and 20%, and 100% imbalance (single-phase) operations by 6%, 12% and 73%, respectively. In addition, it is worth mentioning that single-phase operation generates a pulsating magnetic field according to Eq. (9) and hence higher localized corrosion on the motor casing, see Fig. 1.
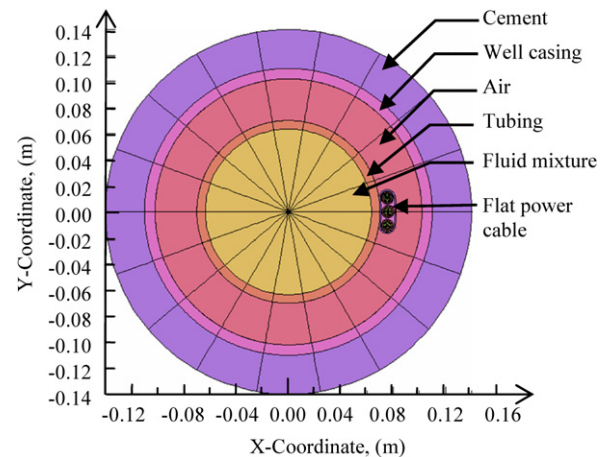

Fig. 15. Oil well cross-sectional view for concentric case including the electric submersible pump flat power cable (dimensions are in m).

Table 3
Configurations of the simulated cross-section of the well

Region	Inner radius (m)	Outer radius (m)
Tubing (steel casing)	0.0635	0.07
Oil layer	0.07	0.102
Well casing	0.102	0.11
Soil layer	0.11	0.14

5.2. Oil well with electric submersible pump power cable models

OPERA-2D is also used to simulate an oil well cross-section with an electric submersible pump cable touching its tubing. This cross-section consists of several layers with different materials which are shown in Fig. 15 and the dimensions are summarized in Table 3.

The used electric submersible pump flat power cable is a 3-phase flat cable with the shown configurations in Fig. 16. The different motor operating conditions are shown in Table 4 with
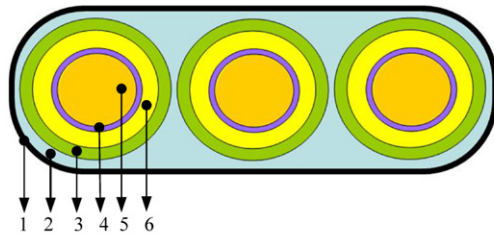
1: Armor: Monel or Galvanic Steel (thickness = 0.0125m)
2: Braid: Synthetic Braid
3: Lead Sheath: Impervious to well Fluids (0.00965m)
4: Polyimide Film: Double (0.0057m)
5: Conductor: Solid Bare Copper (0.00547m)
6: Insulation: High Dielectric: Modulus EPDM Rubber (0.0077m)

Fig. 16. Configuration and parameters of the electric submersible pump flat power cable.

Table 4
Simulated line currents in A (rms)

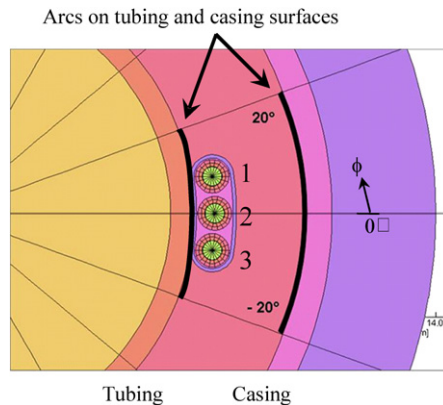| Conductor No.	Balanced case	Single phasing
1	$100\angle 0°$	0
2	$100\angle 120°$	$173.2\angle 0$
3	$100\angle 240°$	$-173.2\angle 0$

Fig. 17. Configuration of the oil well with power flat cable.

their operating current flowing in the cable for each condition. These results describe the distribution of the magnetic-flux density (B) and the current-density (J) at the well casing and its tubing.

Different oil well models have been simulated and studied. They include the simulations of a concentric oil well model and another eccentric well all with the same flat power cable. Also, the simulations included the concentric oil well model but with a round cable. The magnetic-flux density profiles and the current density profiles are plotted and discussed along the following sections.

Figs. 15 and 17 show the concentric case of oil well model. In the concentric case tubing and casing have been centered at the origin. For the eccentric case, the well casing is shifted by 0.015 m to the left.

Figs. 18(a) and 18(b) illustrate the current density profiles along the arcs on the tubing and well casing (see Fig. 17), respectively. The current density has its minimum values near the middle of the cable, i.e. at zero angle. This is due to the cancel-
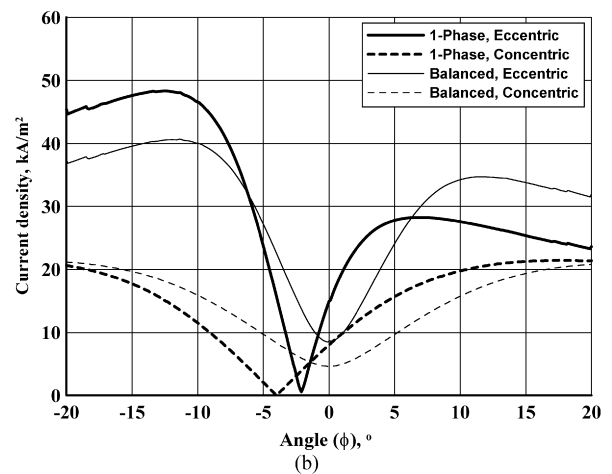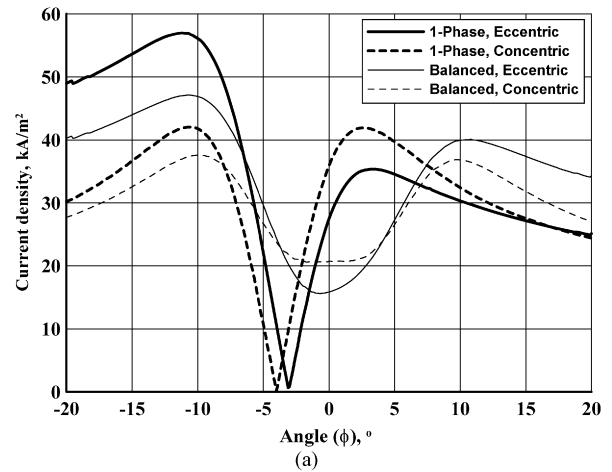

(a)

(b)

Fig. 18. Eddy-current density profiles for flat cable under balanced and single-phase operations on: (a) tubing outer surface and (b) casing inner surface.
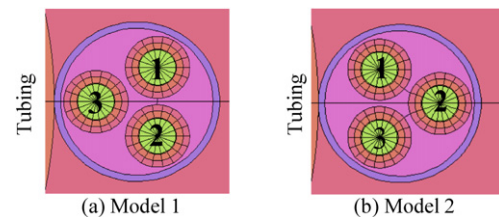
Fig. 19. Configurations of the oil well with power round cables.

lation of the magnetic flux generated by the other conductors. Due to the closer casing (by 0.015 m), in the eccentric case, the magnetic-flux density at the casing has higher values than that of the concentric case. In addition, the eddy-current density at the tubing in the eccentric case is higher than that of the concentric case due the same aforementioned reason. For the single-phase case and referring to the concentric case, the peak value of the eddy-current density increases by 36% and 125% at the tubing and the well-casing surfaces, respectively. The corresponding values for the balanced case are 25% and 92%, respectively. On the other hand, the peak value of the eddy-current density under single-phasing and eccentric case is higher at the tubing surface by 18% compared to that at the well casing.

Fig. 20. Eddy-current density profiles on tubing outer surface and casing inner surface for balanced and single-phase operations for round cable model 1.

Fig. 21. Eddy-current density profiles on tubing outer surface and casing inner surface for balanced and single-phase operations for round cable model 2.

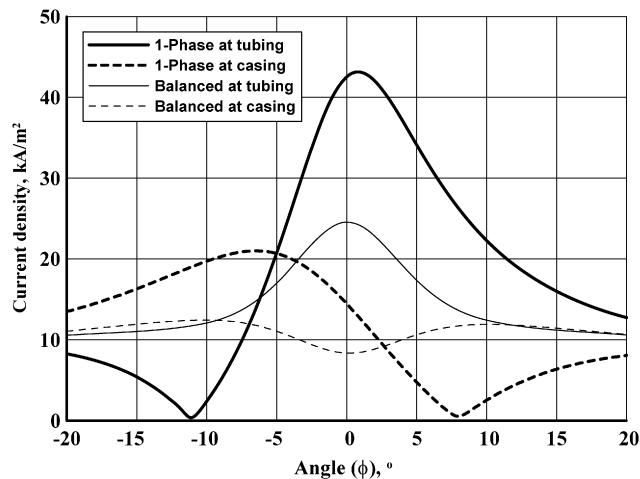It can be observed from Fig. 18(a) that the single phase operating condition has the highest value at the well tubing in the eccentric case and considered to be the worst case among the others. On the other hand, the balanced operating condition is the case of the lowest effect. The other type of cables used for electric submersible pump motors is the round cable shown in Fig. 19.

However, due to the limited space inside the well casings, flat cables normally represent up to 99% of the total electric submersible pump power cable length, while the rest (top side) is of the round-cable type. The same concentric oil well model is built but this time with a round cable. This round cable is similar to the flat cable in terms of conductors' sizes and insulation types.

Fig. 20 shows the profiles of the eddy-current density at the well tubing and casing of the concentric well type for operating conditions, balance and single phasing for cable model 1, see Fig. 19(a). For the single phasing case, the faulty phase was conductor number 1. As expected the current density has a higher peak value than that of the balanced operation.

Comparing the results shown in Fig. 20 with the previous current-density profiles in the case of the concentric oil well with flat cable (shown in Fig. 18), it has been found that the use of round cable reduces the current density on both the well tubing and the well casing. This is attributed to magnetic field cancellation for round cable as a result of the symmetrical arrangement "equilateral triangle". Due to the decrease of the magnetic-flux density with the distance, the current density is lower at the casing compared to that at the tubing. The profiles of the current density at the well tubing opposite to conductor #3 have peaks due to the very narrow separation between that conductor and the tubing.

The other possibility for the round cable to be attached to the well tubing is to have two conductors close the tubing and the third one away as shown in Fig. 19(b). For the single-phase case, the peak value of the eddy-current density at the tubing for model 1 is higher than that for model 2 by 44%. Therefore, the arrangement of the cores of the round cable with respect to the tubing plays an important role in controlling the heating effect.
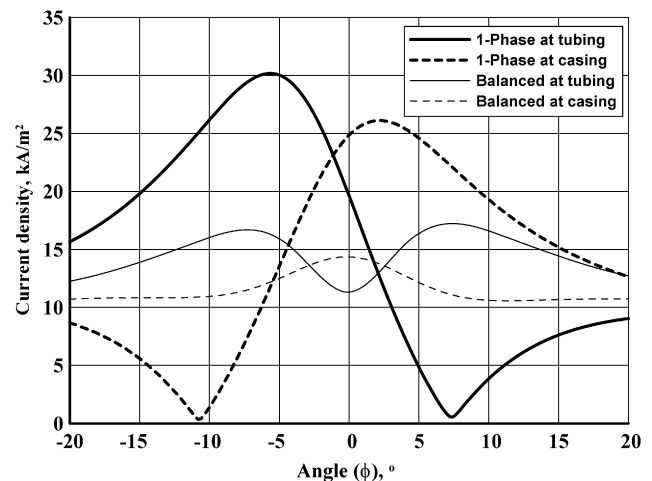
The current density at the well casing for the round cable is shown in Fig. 21 for the normal (balanced) and the single-phasing operating conditions.

The current density profile of the balanced operation tends to be symmetric and that is because the equal current amplitudes in the three phases in addition to symmetric construction of the cable. On the other hand, the single-phase case records the highest value.

Generally, the round cable can be used instead of the flat cable in the oil wells in supplying the electric submersible pump motor to minimize the effects of the eddy-current density and the heating at the well tubing and well casing.

6. Conclusions

Heating tests were performed on a reduced-scale electric submersible pump motor casing to measure its surface temperature profiles due to the ohmic losses caused by the copper losses and the circulation of eddy currents under balanced, unbalanced and single-phasing conditions. The results showed that the single-phasing operation gives the highest temperature rise with time.

The magnetic-flux density test was also conducted on the reduced-scale electric submersible pump motor to measure the magnetic-flux density components generated by the motor under the above-mentioned three conditions at different locations around the motor. It was found that the highest magnetic-flux density appeared in the z-direction (radial). In addition, the results revealed that the magnetic-flux density for single-phase condition is the highest, i.e. higher localized magnetic-flux density or heating and hence higher corrosion rate.

Simulation results for a full-scale electric submersible pump oil well showed that the eccentric case of the motor casing or the well tubing with respect to the well casing gives higher magnetic-flux density at well tubing and casing compared to those for the concentric case. Moreover, the current density and magnetic flux densities at well tubing are higher than those at the well casing. Round cables can be used instead of the flat ones to minimize the magnetic-flux density at the well tubing

and casing, i.e. the heating effect. Moreover, the normalized simulation results of the magnetic flux-density component for the reduced-scale motor were compared by those measured under the same operating conditions and good agreement was obtained.

Finally, it can be concluded that the long-term abnormal operation of the electric submersible pump system, especially with eccentricity, can result in localized heating effects by means of eddy currents. Where the single-phasing with eccentricity operation gives the severest case. There is a strong correlation between the eddy-current thermal effect and the severe localized corrosion of electric submersible pump system. Since corrosion is a multi-factor phenomenon, it is not possible to provide a clear indication about the acceptable levels of imbalance to mitigate it. However, it is highly recommended to use round power cables and not to operate the electric submersible pump system under single-phase condition.

References

[1] A.K. Samant, Corrosion problems in oil industry need more attention, Oil and Natural Gas Corporation Ltd., 18 Feb. 2003.

[2] UNIFIED FACILITIES CRITERIA (UFC), Operation and maintenance: Cathodic protection systems, DRAFT UFC 3-570-06, 1 July 2001.

[3] B.S. Wyatt, Advanced systems of over line assessment of coatings and cathodic protection, in: UMIST Cathodic Protection Conference, Manchester, UK, 10–11 Feb. 2003, pp. 1–15.

[4] Ferrous pipeline corrosion processes, detection and mitigation, Office of Pipeline Safety, US Department of Transportation, Technical Report No. OPS-TR-71-001, Oct. 1971.

[5] Mitigation of alternating current and lightning effects on metallic structures and corrosion control systems, NACE Standard RP0177-2000.

[6] R.J. McKay, R. Worthington, Corrosion Resistance of Metals and Alloys, Reinhold Publishing, New York, 1936.

[7] A. Francis, Introduction to Oil and Gas Technology, third ed., Prentice Hall, 1989.

[8] R.D. Findlay, An algorithm for the determination of eddy-current losses and temperatures in a conductor subjected to high-frequency magnetic-flux variations, Proceedings of the IEEE 70 (11) (Nov. 1982) 1368–1370.

[9] S.V. Kulkarni, J.C. Olivares, R. Escarela-Perez, V.K. Lakhiani, J. Turowski, Evaluation of eddy-current losses in the cover plates of distribution transformer, IEE Proceedings—Science, Measurement and Technology 151 (5) (4 Sept. 2004) 313–318.

[10] O. Bíró, K. Preis, On the use of the magnetic vector potential in the finite element analysis of three-dimensional eddy currents, IEEE Trans. on Magnetics 25 (4) (July 1989) 3145–3159.

[11] L. Turner, R. Lari, Developments in eddy-current computation with EDDYNET, IEEE Transactions on Magnetics 19 (6) (Nov. 1983) 2577–2580.

[12] Z. Wang, X. Yang, Y. Wang, W. Yan, Eddy current and temperature field computation in transverse flux induction heating equipment, IEEE Trans. on Magnetics 37 (5) (2001) 3437–3439.

[13] X. Yang, Y. Wang, W. Yan, The use of neural networks combined with fem to optimize the coil geometry and structure of transverse flux induction equipments, IEEE Trans. Appl. Supercond. 14 (2) (June 2004) 1854–1857.

[14] J.C. Olivares, R. Escarela-Perez, S.V. Kulkarni, F. de León, E. Melgoza-Vasquez, O. Hernández-Anaya, Improved insert geometry for reducing tank-wall losses in pad-mounted transformers, IEEE Trans. Power Delivery 19 (3) (July 2004) 1120–1126.

[15] J.C. Olivares, R. Escarela-Perez, S.V. Kulkarni, F. de Leónd, M.A. Venegas-Vega, 2D Finite-element determination of tank wall losses in pad-mounted transformers, Electric Power Systems Res. 71 (2004) 179–185.

[16] J. Kvarekval, R. Nyborg, Formation of multilayer iron sulfide films during high temperature CO2/H2S corrosion of carbon steel, NACE International Corrosion 99, paper No. 3339, 2003.

[17] D.H. Mesa, A. Toro, A.P. Tschiptschin, The effect of testing temperature on corrosion-erosion resistance of martensic stainless steels, in: WEAR, vol. 255, Elsevier, 2003, pp. 139–145.

[18] S.J. Al-Hassan, G.J. Fonder, P.M. Singh Role of thermal excursions on sulfidation of carbon steel, NACE International Corrosion 99, paper No. 280, 1999.

[19] P.C. Sen, Principles of Electric Machines and Power Electronics, second ed., John Wiley & Sons, Ltd., UK, 1997.

[20] Grundfos Management A/S, Poul Due Jensens Vej 7, DK-8850 Bjerringbro, Denmark. Available: http://www.grundfos.com.

[21] "User Manual of Magnetic Field Sensor # Mag-03MSS and Mag-03PSU", Bartington Instruments Ltd., England. Available: http://www.bartington.com.

[22] User Manual of Vector Fields Software Package. Available: http://www.vectorfields.com.

[23] J. Lähteenmäki, Design and voltage supply of high-speed induction machines, Ph.D. Dissertation, ACTA Polytechnica Scandinavica, Electrical Engineering Series No. 108, 2002.

[24] Y. Lee, H. Lee, S. Hahn, Temperature analysis of induction motor with distributed heat sources by finite element method, IEEE Trans. on Magnetics 33 (2) (March 1997) 1718–1721.

Ibrahim A. Metwally (IEEE M'93–SM'04) was born in 1963. He received the B.Eng. degree in electrical engineering (Hons.), the M.Eng. degree in high-voltage engineering, and the Ph.D. degree in high-voltage engineering from Mansoura University, Mansoura, Egypt, in 1986, 1990, and 1994, respectively. The Ph.D. degree was received in collaboration with Cardiff University, Cardiff, U.K.

He is currently a Professor with the Department of Electrical Engineering, Mansoura University. He has been seconded to the Department of Electrical and Computer Engineering, College of Engineering, Sultan Qaboos University, Muscat, Oman since August 2002. From 2000 to 2002 and in the summers of 2003–2007, he joined the University of the Federal Armed Forces, Munich, Germany, as a Visiting Professor. His areas of research include oil- and gas-flow electrification in both electric power apparatus and pipelines, measurements of fast impulse voltages and currents, line insulators and zinc-oxide surge arresters, coronas on overhead transmission lines, impulse voltage characterization and modeling of electrical machines, particle-initiated breakdown in gas-insulated switchgear (GIS) and gas-insulated transmission lines (GITL), power quality, stray-current corrosion in the oil industry, and hazards of lightning strikes to buildings, overhead power lines, and aircrafts.

He is a Fellow of the Alexander von Humboldt (AvH) Foundation, Bonn, Germany, a Senior Member in the Institute of Electrical and Electronics Engineers (IEEE) and a Member of the International Electrotechnical Commission (IEC). He has published 100 papers, where about half of them archived in highly reputed international journals. He has completed 12 industrial projects in UK, Egypt, Germany and Oman, and 8 support services (consultations) in Oman. He was awarded both the First Rank of the National Prize in Engineering Sciences in 1998 and 2004, and the Late Prof. Dr.-Ing. M. Khalifa's Prize in Electrical Engineering in 1999 and 2005 from the Egyptian Academy of Scientific Research and Technology. He has been a regular peer reviewer for IEEE Transactions on Dielectrics and Electrical Insulation, Power Delivery and Electromagnetic Compatibility, IET Generation, Transmission & Distribution, Journal of Electric Power Systems Research, and European Transactions on Electrical Power. His biographical profile was published in Who's Who in Science and Engineering in 2001.

Adel Gastli (IEEE S'89–M'93– SM'00) received the B.Sc. degree in Electrical Engineering from National School of Engineering of Tunis, Tunisia in 1985. He received the M.Sc. and Ph.D. degrees from Nagoya Institute of Technology, Japan in 1990 and 1993 respectively. He joined the R&D Department at Inazawa Works (elevators and escalators) of Mitsubishi Electric Corporation in Japan from April 1993 to Aug. 1995. He is currently an Associate Professor of Electrical Engineering at Sultan Qaboos University, Muscat, Oman. His current research interests include electrical machines, power electronics, drives, power quality, renewable energy, power system analysis, and stray current corrosion in oil industry.